Sustainable Energy & Fuels

ROYAL SOCIETY OF CHEMISTRY

PAPER

View Article Online
View Journal | View Issue

Cite this: *Sustainable Energy Fuels*, 2023, 7, 1311

Construction of strongly coupled 2D–2D SnS_2/CdS S-scheme heterostructures for photocatalytic hydrogen evolution†

Xiaoyu Chen, Zhi Han, Zonghao Lu, Tingting Qu, Ce Liang, Yu Wang, Bin Zhang,* Xijiang Han* and Ping Xu*

The fabrication of neoteric photocatalysts with high-efficiency charge separation for the solar-driven hydrogen evolution reaction (HER) remains a challenge. The construction of strongly coupled two-dimensional (2D)–2D heterostructures facilitates charge spatial migration due to the regulation of the interlayer forces and electronic structures. In this work, we demonstrate novel 2D–2D SnS_2/CdS heterostructures by loading SnS_2 nanosheets (SnS_2 NSs) onto CdS nanosheets (CdS NSs). The SnS_2/CdS heterostructures possess close face-to-face contact and strongly coupled interactions to improve the charge transfer kinetics, and the loading of SnS_2 can enhance light absorption and suppress the photocorrosion of CdS. The optimized S-scheme SnS_2/CdS heterostructures exhibit excellent photocatalytic hydrogen evolution activity in lactic acid sacrificial solution under visible light ($\lambda \geq 420$ nm), affording the highest hydrogen evolution rate on SnS_2/CdS heterostructures with 35 wt% SnS_2 (5.18 mmol g^{-1} h^{-1}), which is approximately 6-fold higher than that of pure CdS NSs (0.87 mmol g^{-1} h^{-1}). In addition, a highest apparent quantum efficiency (AQE) of 59.3% was obtained at 420 nm. When methanol was used as the sacrificial agent, the hydrogen production rate reached 3.27 mmol g^{-1} h^{-1} and methanol was oxidatively reformed into methoxymethanol (CH_3OCH_2OH). This work provides a feasible method for designing strongly coupled 2D–2D heterostructure photocatalysts for energy storage and conversion applications.

Received 13th December 2022
Accepted 25th January 2023

DOI: 10.1039/d2se01717b

rsc.li/sustainable-energy

1. Introduction

Due to over-reliance on traditional fossil fuels, there are great concerns regarding environmental pollution and energy shortage.[1] Solar-fuel conversion is one of the best ways to achieve of energy supply revolution and sustainable development.[2] Photocatalytic water splitting powered by solar energy is one of the technologies with the greatest potential to alleviate the above problems by producing green hydrogen energy.[3] Therefore, more attention has been focused on the intensive exploration of photocatalysts with reactive sites and excellent durability for elevating the conversion efficiency of solar-to-hydrogen energy.[4,5]

Among the hydrogen-evolving semiconductors, cadmium sulfide (CdS) is a prominent photocatalyst with a suitable band gap (~2.4 eV) for utilizing visible light and an appropriate conduction band position for reducing protons to hydrogen.[6] However, pure bulk CdS has a series of inherent shortcomings including photocorrosion and inevitable annihilation of photogenerated electron–hole pairs.[7] As a result, it has always been challenging to design outstanding CdS-based photocatalysts with prominent stability for the hydrogen evolution reaction (HER) in water splitting. Compared to bulk CdS, two-dimensional (2D) CdS NSs possess a large specific surface area and more active sites, which are not only conducive to the rapid migration of photogenerated carriers from the bulk phase to the surface but are also beneficial for constructing 2D–2D layered heterostructures with face-to-face contact and plentiful interfacial contact.[8–10] Among the CdS-based heterostructure materials, considerable research efforts have been devoted to designing CdS-based S-scheme photocatalytic systems, such as CdS/WO_3,[11] CdS/TiO_2,[12] CdS/$CuWO_4$,[13] g-C_3N_4/CdS,[14] CdS/$BiVO_4$,[15] CdS/ZnO,[16] FeOOH/CdS,[17] and CdO/CdS,[18] since S-scheme heterostructures have a unique charge transfer path that can suppress the photocorrosion and retain the high reducibility of the photogenerated electrons.[19] Moreover, integration with other conductive materials to construct S-scheme heterostructures is beneficial for improving the photocatalytic hydrogen evolution performance.[20] Thus, the exploration of 2D CdS-based S-scheme photocatalysts with well-defined structures and remarkable activity is of paramount significance. Inspired

MIIT Key Laboratory of Critical Materials Technology for New Energy Conversion and Storage, School of Chemistry and Chemical Engineering, Harbin Institute of Technology, Harbin 150001, China. E-mail: zhangbin_hit@aliyun.com; hanxijiang@hit.edu.cn; pxu@hit.edu.cn

† Electronic supplementary information (ESI) available: Fig. S1–S14 and Tables S1 and S2. See DOI: https://doi.org/10.1039/d2se01717b

by this, we set out to find another suitable 2D material to fabricate CdS-based heterojunction photocatalysts through a strong electronic coupling effect.[21,22]

Recently, tin disulfide (SnS_2) with a narrow band gap energy of 2.2–2.4 eV and promising visible-light response was identified as a conspicuous n-type semiconductor for the photocatalytic reaction.[23,24] Vacancy defect engineering was utilized to design dually modified MoS_2/SnS_2 S-scheme heterojunction photocatalysts for the photo-reduction of Cr(VI) and the photodegradation of organic dyes.[25] 2D SnS_2/TiO_2 heterostructures with exposed high-energy (001) and low-energy (101) facets were constructed for the enhanced photocatalytic reduction of CO_2 into CH_4.[26] 2D thin hexagonal SnS_2 nanosheets were fabricated on 2D g-C_3N_4 nanosheets by simple ultrasonic and calcination methods to generate SnS_2/g-C_3N_4 heterostructures with tight interface matching between facets and excellent charge separation efficiency, which is beneficial for U(VI) removal under actual sunlight irradiation.[27] So far, there have been few reports about 2D–2D SnS_2/CdS heterostructures in the field of the sunlight-driven HER through water splitting. Moreover, according to the literature, it is feasible to construct an S-scheme heterostructure between SnS_2 and CdS, since the conduction band and valence band of SnS_2 nanosheets match well with those of CdS nanosheets.[28,29]

Guided by the above strategies, herein, we report the construction of a 2D–2D strongly coupled SnS_2/CdS heterostructure photocatalyst for enhanced hydrogen evolution in solar-driven water splitting. This unique face-to-face contact effectively promotes charge transfer, and the loading of SnS_2 NSs can improve the visible-light absorption and suppress the photocorrosion of the CdS NSs. As a result, the highest hydrogen evolution rate of 5.18 mmol g^{-1} h^{-1} was obtained with lactic acid as the sacrificial agent under visible-light irradiation, with the highest apparent quantum efficiency (AQE) of 59.3% at 420 nm. Furthermore, when methanol was used as the sacrificial agent, the hydrogen production rate was 3.27 mmol g^{-1} h^{-1}, where methanol can be transformed into CH_3OCH_2-OH. This research may provide an innovative strategy for the design of SnS_2 and CdS based photocatalysts with enhanced water-splitting performance under visible-light irradiation.

2. Experimental section

2.1 Synthesis of CdS nanosheets

CdS nanosheets (CdS NSs) were synthesized through a hydrothermal method.[30] Specifically, 0.8 g of $Cd(Ac)_2 \cdot 2H_2O$ and 0.87 g of NH_2CSNH_2 were dispersed in 30 mL of ethylenediamine under magnetic stirring and then the solution was transferred to a 50 mL Teflon-lined autoclave and maintained at 100 °C for 12 h. After cooling naturally to room temperature, the yellow powder was centrifuged and washed with distilled water, and then dried in air at 60 °C.

2.2 Synthesis of 2D–2D SnS_2/CdS heterostructures

Different amounts of $SnCl_4 \cdot 5H_2O$ and 1.051 g of citric acid monohydrate were added to 40 mL H_2O under magnetic stirring for 30 min. Next, 0.1 g of the as-prepared CdS NSs and 0.6 g dicyandiamide were added to the above solution under magnetic stirring for 30 min. The solution was transferred to a 100 mL Teflon-lined autoclave and maintained at 180 °C for 12 h. The loading amount of SnS_2 nanosheets (SnS_2 NSs) was adjusted by changing the amounts of $SnCl_4 \cdot 5H_2O$ added, and these different SnS_2/CdS heterostructures were denoted as SnS_2/CdS-x ($x = 5, 15, 25, 35, 45$, corresponding to the loadings of 5%, 15%, 25%, 35%, 45% in weight of the SnS_2 NSs). For the synthesis of pure SnS_2 NSs, the above steps can be performed again without adding pure CdS NSs.

2.3 Characterization

A JEM-2100F instrument with 200 kV of accelerating voltage was used to obtain transmission electron microscopy (TEM) images. Powder X-ray diffraction (XRD) data were obtained on a D2 PHASER (AXS) X-ray diffractometer with a Cu Kα radiation source (45.0 kV, 50.0 mA). Raman spectra were collected using a micro-Raman spectroscopy system (Renishaw inVia). The N_2 adsorption–desorption isotherms gained from QUADRASORB SI-KR/MP and the surface area of the materials were estimated by Brunner–Emmet–Teller (BET) measurements. X-ray photoelectron spectroscopy (XPS) data was tested by a PHI-5400 ESCA system using an Al Kα radiation source. The standard photoelectron peak of the C 1s at 284.8 eV was used as a reference value to calibrate the binding energy. The Hitachi UH4150 spectrometer was employed to collect the UV-vis absorption spectra. Photoluminescence (PL) spectra were recorded on a PerkinElmer LS 55 spectrometer at an excitation wavelength of 365 nm. The temperature changes and distributions under light illumination were tested by a thermal infrared imager (Fotric 225s, China). The NMR spectra were collected using a Bruker 600 MHz.

2.4 Mott–Schottky measurement

To further investigate the process of photocatalytic hydrogen evolution, Mott–Schottky tests were used to calculate and compare the densities of charge carriers (N_d).[31] The carrier density was calculated using eqn (1):

$$N_d = \frac{2/e_0\varepsilon\varepsilon_0}{d(1/C^2)/dV} \quad (1)$$

where e_0 is the electron charge, ε is the dielectric constant of the semiconductor, ε_0 is the permittivity of the vacuum, C is the capacitance, and V is the applied bias at the electrode.

2.5 Photocatalytic hydrogen production test

Photocatalytic hydrogen production was tested at room temperature in a vacuum-closed gas circulation system (Labsolar 6A, PerfectLight, Beijing, Fig. S1†). Typically, 50 mg of the as-prepared catalyst was dispersed in 100 mL of an aqueous solution containing 10 mL of lactic acid. Before irradiation, the reaction system was vacuum pumped for 30 min, and the yield of hydrogen was detected by gas chromatography (FULI GC9790 II) using Ar as carrier gas. A xenon lamp source of 300 W (PLS-

SXE300, PerfectLight, Beijing, Fig. S1†) with a cutoff 420 nm filter was fixed 10 cm above the liquid level, and other bandpass filters (365, 420, 550, 700 nm) were used to measure the AQE.[32] The AQE was calculated using eqn (2):

$$\mathrm{AQE} = \frac{2 \times \text{the number of evolved } H_2 \text{ molecules}}{\text{the number of incident photons}} \times 100\% \quad (2)$$

2.6 Photoelectrochemical test

The photoelectrochemical measurements were carried out with a standard three-electrode cell on a CHI 660D (CH Instruments, Inc.) electrochemical workstation, with Ag/AgCl as the reference electrode, platinum foil as the counter electrode, and the as-prepared photocatalysts dropped on a fluorine-doped tin oxide (FTO) glass substrate with an effective area of 2×1 cm^2 as the working electrode. The rotating disk electrode was always kept open during the photochemical test. Here, 0.1 M Na_2SO_4 was purged with N_2 and used as the electrolyte. Visible light (cutoff 420 nm, PLS-SXE300, PerfectLight, Beijing) was used as the light irradiation source.

2.7 Computational methods

All density functional theory (DFT) calculations were performed on the Vienna *Ab initio* Simulation Package (VASP) by using the PBE exchange-correlation function. The interaction between valence electrons and the ionic core was described by the PAW pseudo-potential. Geometry optimization was conducted with a cutoff energy of 400 eV. We considered the GGA+U approach and the van der Waals forces were considered using the DFT-D3 method. The three layers of atoms on the surface were allowed to relax until the magnitude of all residual forces was less than 0.02 eV. Ionic relaxations were carried out under conventional energy (10^{-5} eV). The Monkhorst–Pack *k*-point mesh of $3 \times 3 \times 1$ was used to calculate the geometry optimization.

3. Results and discussion

The strongly coupled 2D–2D SnS_2/CdS heterostructures with enhanced photocatalytic hydrogen evolution performance were fabricated *via* a hydrothermal method (Fig. 1a). The optical images of pure CdS NSs, SnS_2/CdS heterostructures, and pure SnS_2 NSs are shown in Fig. S2,† where the color changed from light yellow to orange. The prepared CdS nanoflowers were composed of ultrathin CdS NSs (Fig. 1b) and the 2D–2D SnS_2/CdS heterostructures were constituted by SnS_2 NSs inserted into the lacuna of CdS NSs assemblies to form the face-to-face strong contact (Fig. 1c). As shown in Fig. 1d, the CdS NSs mainly exposed (002) crystal planes with a spacing of 0.332 nm, and the mainly exposed crystal face of SnS_2 NSs was the (100) plane with a spacing of 0.313 nm.[33] Furthermore, the selected area electron diffraction (SAED) pattern (Fig. 1e) verified that SnS_2 NSs were strongly coupled on the surface of CdS NSs, and suggested that CdS and SnS_2 NSs exposed their (002) and (100) crystal faces, respectively. Moreover, the elemental mappings (Fig. 1f–i) exhibited that the Cd, Sn, and S elements were uniformly

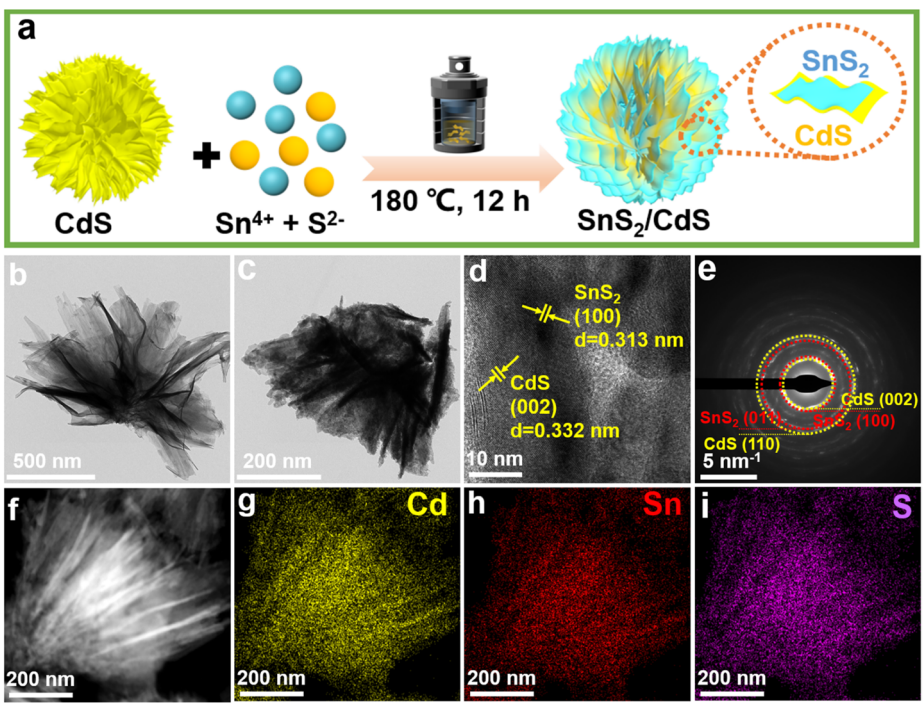

Fig. 1 (a) Schematic representation of the preparation process of 2D–2D SnS_2/CdS heterostructures. (b and c) TEM images of CdS NSs and 2D–2D SnS_2/CdS heterostructures. (d) HRTEM images, (e) SAED pattern, and (f–i) the corresponding EDX mapping images of 2D–2D SnS_2/CdS heterostructures.

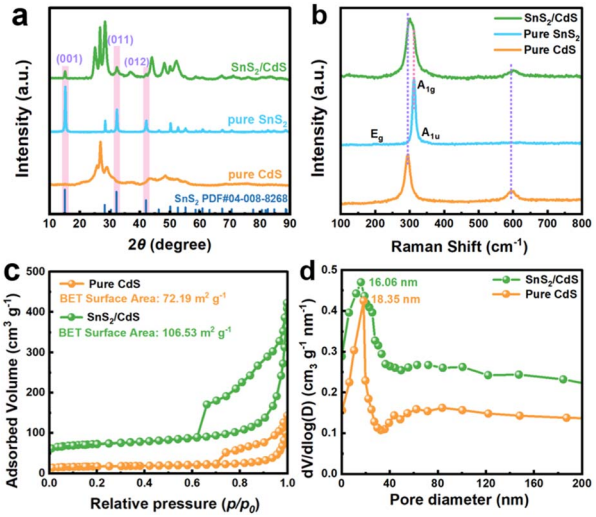

Fig. 2 (a) XRD patterns, (b) Raman spectra, (c) nitrogen sorption–desorption isotherms and (d) the corresponding pore size distribution plots of the pure CdS and 2D–2D SnS_2/CdS heterostructures.

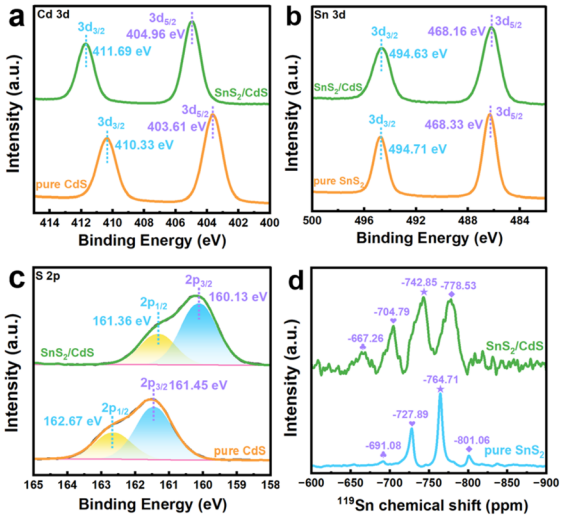

Fig. 3 (a) Cd 3d XPS peaks, (b) Sn 3d XPS peaks, (c) S 2p XPS peaks of the pure CdS NSs and 2D–2D SnS_2/CdS heterostructures, and (d) ^{119}Sn MAS NMR spectra of pure SnS_2 and SnS_2/CdS heterostructures.

distributed. For pure SnS_2, the nanosheets tended to manifest into hexagonal structures (Fig. S3†).

X-ray diffraction (XRD) patterns of pure CdS, SnS_2/CdS heterostructures, and pure SnS_2 are shown in Fig. 2a. For pure CdS NSs, the diffraction peaks can be indexed to the hexagonal CdS phase (PDF# 01-070-2553).[34] Compared with pure CdS and SnS_2 NSs, the diffraction peaks of SnS_2/CdS heterostructures at 15.13, 28.45, and 42.22° are ascribed to the (001), (011), and (012) crystal faces of SnS_2 (PDF# 04-008-8268).[35] From Raman spectra (Fig. 2b), the characteristic peaks of SnS_2/CdS heterostructures were slightly blue-shifted compared with those of pure CdS NSs, which is powerful evidence for the formation of strongly coupled contact between SnS_2 and CdS. For pure SnS_2 NSs, the out-of-plane A_{1g} mode at ~314 cm^{-1} is the most prominent, while the peaks of E_g and A_{1u} modes are extremely weak.[36] Notably, the Raman band of SnS_2/CdS heterostructures around 300 cm^{-1} became broadened, which proved the existence of SnS_2 NSs. The N_2 sorption–desorption isotherms are typical type-IV isotherms. The Brunauer–Emmett–Teller (BET) surface areas of CdS NSs, SnS_2/CdS heterostructures, and SnS_2 NSs are 72.19, 106.53, and 132.18 m^2 g^{-1}, and the Barrett–Joyner–Halenda (BJH) pore sizes (Fig. 2d and S4†) of the three are 16.06, 18.35, and 23.62 nm, respectively. This morphology change of SnS_2/CdS heterostructures is helpful to provide more active sites for photocatalysis.[37,38]

X-ray photoelectron spectroscopy (XPS) measurements were performed to study the elemental compositions and chemical environments of the samples. Compared with pure CdS NSs, there were characteristic peaks of the Sn element in the SnS_2/CdS heterostructures from the full-spectrum scan (Fig. S5 and S6†), which implies the loading of SnS_2 NSs on the CdS NSs. In detail, the Cd 3d peaks of SnS_2/CdS heterostructures (Fig. 3a) shifted from 410.33 and 403.61 eV to 411.69 and 404.96 eV as compared to pure CdS NSs, indicating that the electron density of CdS NSs decreased with the decoration of the SnS_2 NSs.[39] Analogously, the Sn 3d peaks of SnS_2/CdS heterostructures (Fig. 3b) shift from 494.71 and 468.33 eV to 494.63 and 468.16 eV, which imply a strong interaction between SnS_2 and CdS.[40] Moreover, as exhibited in Fig. 3c, the peaks at 161.36 and 160.13 eV affiliated with S 2p1/2 and S 2p3/2 of SnS_2/CdS heterostructures moved to lower binding energies as compared with pure CdS NSs, further substantiating the formation of heterostructures.[41]

The solid-state ^{119}Sn NMR tests were also carried out to reveal the chemical structure of SnS_2/CdS heterostructures (Fig. 3d). The characteristics of the main line indicate that the Sn atoms in pure SnS_2 and SnS_2/CdS heterostructures have different atomic environments at the NMR scale, that is, a slight disorder exists in SnS_2/CdS heterostructures. Pure SnS_2 NSs exhibited four characteristic peaks at −691.08, −727.89, −764.71, and −801.06 ppm, corresponding to the Sn(IV)–S bonds.[42,43] The four peaks clearly show the presence of the four distinct Sn sites in the materials. For SnS_2/CdS heterostructures, the Sn(IV) peaks were slightly shifted to up-field with lower chemical shifts, suggesting that the electron density around the Sn atom increased. It is worth noting that the intensities of the peaks at −667.26 ppm and −778.53 ppm in the SnS_2/CdS heterostructures were significantly stronger than those in pure SnS_2, indicating that there was strong interfacial interaction between CdS and SnS_2, resulting in increased Sn(IV) content.[44–47] In addition, in the SnS_2/CdS heterostructures, the peak width of the four characteristic peaks was significantly wider than those of pure SnS_2, which is because the Sn sites act as the connecting anchors at the interface between CdS and SnS_2. The above results reveal that there is strong coupling between SnS_2 and CdS.

The light-harvesting performances (Fig. 4a and S7a†) of pure CdS NSs and SnS_2/CdS heterostructures were tested by UV-vis absorption spectroscopy. The SnS_2/CdS heterostructures showed enhanced light absorption from 700 to 800 nm as

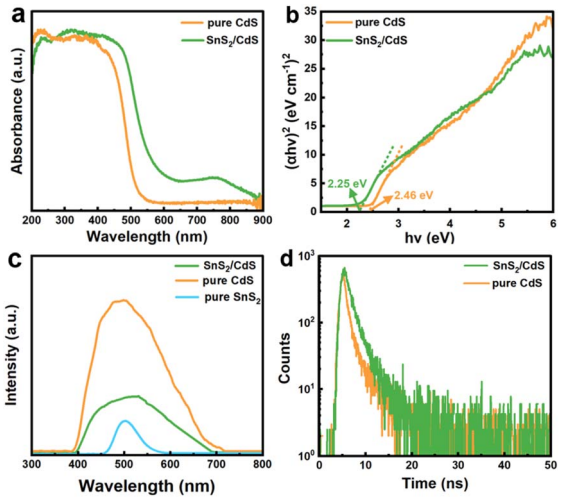

Fig. 4 (a) UV-vis absorption spectra, (b) optical band gaps, (c) photoluminescence spectra, and (d) time-resolved transient photoluminescence decay spectra of the pure CdS NSs and 2D–2D SnS_2/CdS heterostructures.

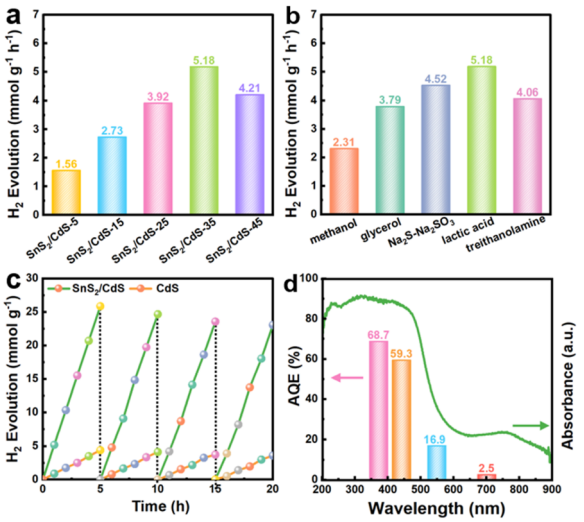

Fig. 5 (a) H_2 evolution rates of SnS_2/CdS heterostructures with different amounts of SnS_2 NSs; (b) a comparison of photocatalytic hydrogen production activities with different sacrificial agents; (c) cycling tests of photocatalytic H_2 evolution under visible light ($\lambda \geq 420$ nm); (d) UV-vis light absorption and the corresponding wavelength-dependent AQE of SnS_2/CdS heterostructures.

compared with pure CdS NSs. The optical bandgaps of pure CdS NSs and SnS_2/CdS heterostructures were calculated from linear transformations of absorption curves (Fig. 4b). Since the pure SnS_2 NSs possess a narrow band gap (Fig. S7b†), the band gap of SnS_2/CdS heterostructures decreased to 2.25 eV, lower than that of pure CdS NSs (2.46 eV), which may substantially enhance the utilization of solar energy and elevate the photocatalytic activity.[48,49] Photoluminescence spectroscopy (PL) was carried out to study the separation ability of photogenerated electron–hole pairs (Fig. 4c). The PL intensities of SnS_2/CdS heterostructures were lower as compared to pure CdS NSs because pure SnS_2 NSs have very low PL intensity, suggesting that SnS_2/CdS heterostructures have a higher carrier separation efficiency.[50] Furthermore, to study the migration dynamics of the carriers, the time-resolved transient photoluminescence (TRPL) decay spectra (Fig. 4d and S8†) were employed. Table S1† records the relevant data, where τ is the lifetime and A is the corresponding magnitude. Accordingly, the pure SnS_2 NSs have the longest positron lifetime (27.94 ns), and the positron lifetime of SnS_2/CdS heterostructures (2.12 ns) is longer than that of pure CdS NSs (1.80 ns), verifying that the introduction of SnS_2 NSs can elevate the separation efficiency of photogenerated carriers and prolong the lifetime of electrons.[51]

The photocatalytic hydrogen evolution performances were firstly measured in deionized (DI) water with lactic acid as a scavenger under visible-light irradiation ($\lambda \geq 420$ nm). Benefiting from the tight face-to-face contact between SnS_2 NSs and CdS NSs, the SnS_2/CdS heterostructures with a strong electronic coupling effect showed outstanding photocatalytic performance. The hydrogen evolution rate of SnS_2/CdS heterostructures with different loading amounts of SnS_2 showed a volcano shape (Fig. 5a). With 35 wt% SnS_2 NSs loaded, the hydrogen production rate of SnS_2/CdS heterostructures can reach up to 5.18 mmol g^{-1} h^{-1}, which is approximately 5.95-fold that of pure CdS NSs (0.87 mmol g^{-1} h^{-1}). Moreover, the SnS_2/CdS heterostructures exhibited remarkable photocatalytic HER performance with different sacrificial agents (Fig. 5b), fully certifying that constructing strongly coupled contacts can provide more active sites and improve the separation efficiency of photogenerated electrons and holes. Particularly, the SnS_2/CdS heterostructures can maintain photocatalytic stability after 20 hours of cycling tests (Fig. 5c), indicating that loading SnS_2 NSs can also favor the suppression of the photocorrosion of CdS. XRD and XPS analyses (Fig. S9†) were carried out on the SnS_2/CdS heterostructures after 20 hours of cycling tests, and there was no change in the valence state of SnS_2/CdS heterostructures. Fig. 5d shows the wavelength-dependent AQE of the 35 wt% SnS_2/CdS heterostructures irradiated at different wavelengths (365, 420, 550, and 700 nm), suggesting that the photocatalytic hydrogen evolution is driven by absorption and photoexcitation. Notably, the highest apparent quantum efficiency (AQE) of SnS_2/CdS heterostructures was 59.3% at 420 nm, which is higher than that of most CdS-based photocatalysts (Table S2†). Based on the above results, the 35 wt% SnS_2/CdS heterostructure not only possessed remarkable photocatalytic performance under ultraviolet light ($AQE_{365\ nm} = 68.7\%$), but also exhibited promising activity under visible light irradiation ($AQE_{420\ nm} = 59.3\%$), proving that loading SnS_2 NSs can promote the light absorption capacity of CdS.

The oxidative reforming of methanol is also an important chemical reaction. Here, when methanol is used as the sacrificial agent, both H_2 and carbon-containing products can be obtained. Fig. 6a shows the hydrogen production rate of SnS_2/CdS heterostructures with methanol as the sacrificial agent, and the hydrogen production rate can reach 3.27 mmol g^{-1} h^{-1}. Moreover, the catalytic activity can remain stable after 20 hours of cycling tests. NMR analysis was used to investigate the types

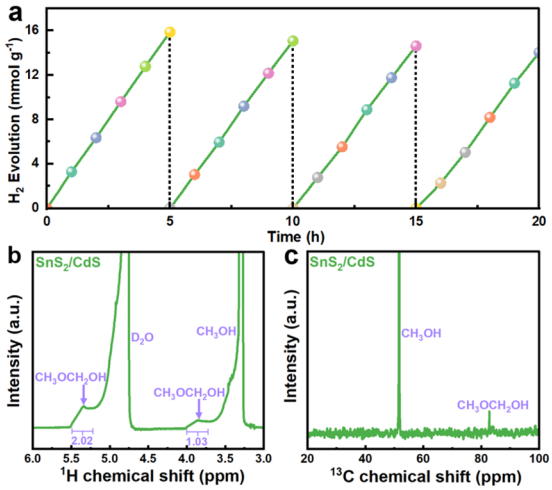

Fig. 6 (a) H_2 evolution rates of SnS_2/CdS heterostructures with methanol as the sacrificial agent. (b) ^{1}H NMR and (c) ^{13}C NMR spectra of the products of photocatalytic reaction with methanol as the sacrificial agent.

of carbon-containing products when methanol was used as a sacrificial agent. From the ^{1}H NMR spectrum (Fig. 6b), there are two characteristic peaks at 3.85 and 5.85 ppm corresponding to CH_3OCH_2OH.[52] Similarly, the peak at 82.8 ppm can also be attributed to CH_3OCH_2OH in the ^{13}C NMR spectrum (Fig. 6c). Therefore, methanol was oxidized to CH_3OCH_2OH along with the photocatalytic hydrogen evolution reaction.

The photoelectrochemical properties can reflect more information about photogenerated carriers. The electrochemical impedance spectroscopy (EIS) Nyquist plots are exhibited in Fig. 7a. The arc radii of SnS_2/CdS heterostructures are smaller than those of pure CdS with and without light irradiation, demonstrating that SnS_2/CdS heterostructures

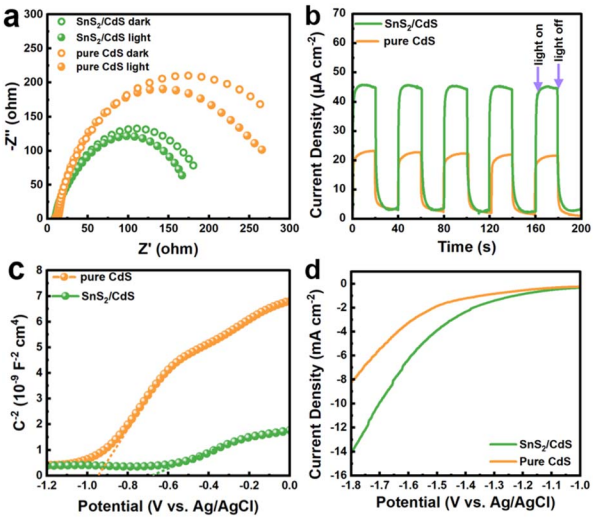

Fig. 7 (a) EIS Nyquist plots, (b) chronoamperometry curves, (c) Mott–Schottky plots, and (d) linear sweep voltammogram curves of pure CdS and SnS_2/CdS heterostructures.

possess smaller interfacial resistance for charge separation.[53] The chronoamperometric curves at an applied constant voltage of 0.6 V in 0.1 M Na_2SO_4 solution under light and dark conditions are displayed in Fig. 7b. In detail, the photocurrent density of SnS_2/CdS heterostructures under visible light ($\sim$45 μA cm^{-2}) is twice that of pure CdS, demonstrating that constructing strongly coupled face-to-face contact is conducive to charge separation and migration.[54] Note that the chronoamperometric responses of both SnS_2/CdS heterostructures and pure CdS maintained stability for several cycles. The carrier density of these photocatalysts can be reflected in the slope of the Mott–Schottky (M–S) curves in Fig. 7c. The SnS_2/CdS heterostructures displayed a smaller slope than that of pure CdS, implying that the SnS_2/CdS heterostructures possessed higher carrier density and the establishment of 2D–2D strong coupled contact can favour the transfer of carriers.[55] From the linear sweep voltammogram (LSV) curves (Fig. 7d), the SnS_2/CdS heterostructures have a smaller overpotential for the hydrogen evolution reaction compared with pure CdS and SnS_2 (Fig. S10†), suggesting that loading SnS_2 NSs can improve the proton reduction ability.[56]

According to the XPS of pure CdS and pure SnS_2, their valence band (VB) positions can be extracted (Fig. S11a and b†). Combining with the optical band gaps, their conduction band (CB) positions can be calculated. Two possible electron transfer mechanisms of SnS_2/CdS heterostructures are shown in Fig. 8a and b. To drive the photocatalytic water splitting reaction, the reduction potential of the bottom of the conduction band must be more negative than that of hydrogen ion to hydrogen (-0.414 V *vs.* NHE at pH = 7). If the SnS_2/CdS heterostructures conform to the type-II electron transfer mechanism, the hydrogen evolution reaction will occur on the SnS_2 conduction band. The conduction band potential of SnS_2 is more positive than the reduction potential of H^+/H_2, and the hydrogen evolution reaction cannot occur on the conduction band of SnS_2, so the SnS_2/CdS heterostructures do not conform to the type-II electron transfer mechanism. In terms of the work function calculated by DFT (Fig. 9a–c), the electron is always transferred from the high Fermi level to the low Fermi level, until the Fermi levels of the two are in equilibrium. From Fig. 8c, the conduction band position of CdS is higher than that of SnS_2, so it can be considered that the electrons at the interface should be transferred from the CdS to SnS_2 until the Fermi levels of the two phases reach equilibrium at the interface. This kind of electron transfer will lead to a decrease in electron density at the interface of CdS and an increase in electron density at the interface of SnS_2, resulting in the potential difference between the two phases and the formation of the built-in electric field at the interface (the direction of the electric field is from CdS to SnS_2).[57] Moreover, the VB of CdS bends upward and the CB of SnS_2 bends downward. Under visible light irradiation, the built-in electric field can induce electron transfer from the SnS_2 conduction band to the CdS valence band. Therefore, the S-scheme heterostructures between CdS and SnS_2 were established. The band bending can weaken the energy barrier, which is beneficial for enhancing the proton reduction ability of the CB of the CdS for the photocatalytic hydrogen evolution reaction. Simultaneously, the holes were

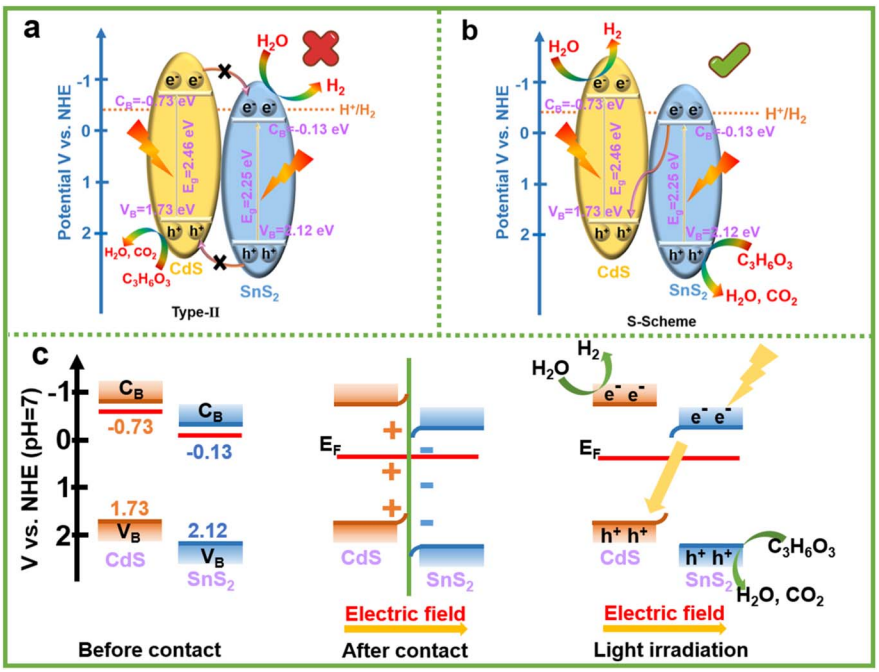

Fig. 8 (a) Type-II and (b and c) S-scheme illustration of the possible charge transfer processes in the SnS_2/CdS heterostructures.

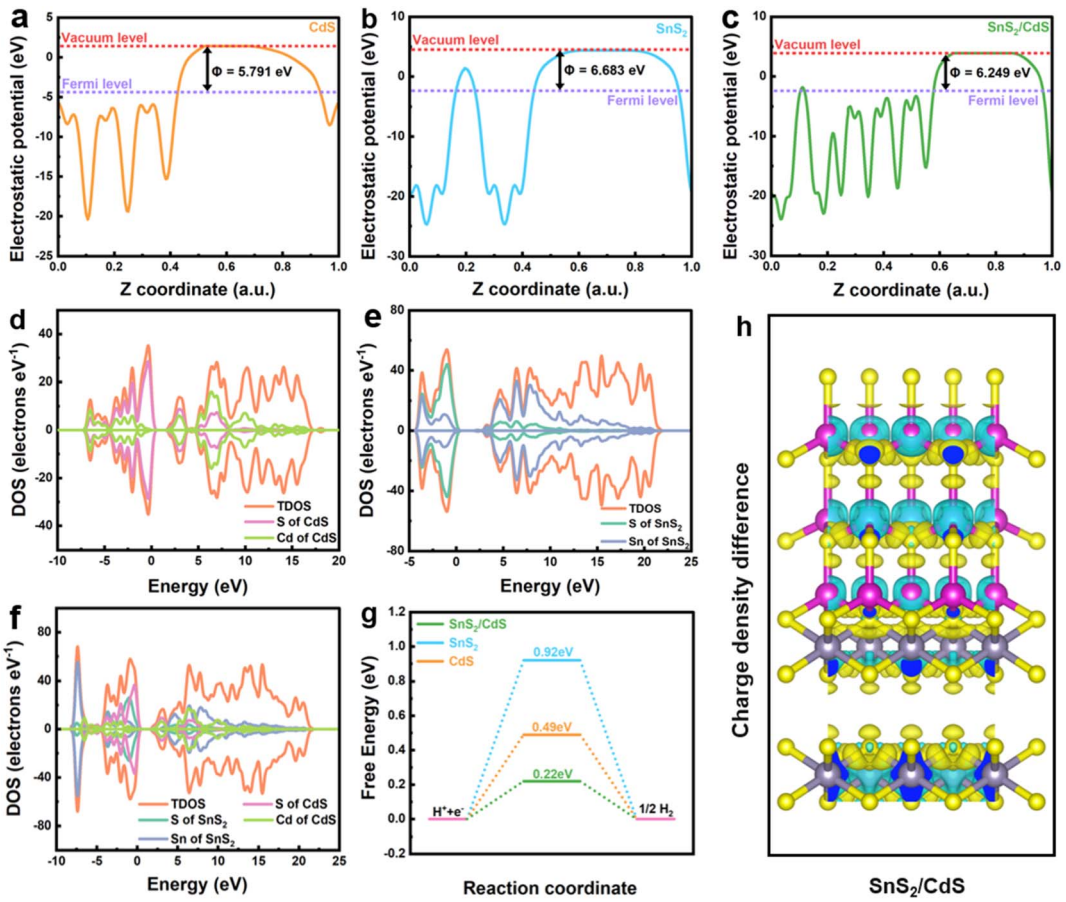

Fig. 9 (a–c) Work function and (d–f) density of state plots, (g) hydrogen adsorption free energy diagram of CdS (002), SnS_2 (100), and SnS_2/CdS heterostructures interface, and (h) charge density difference diagram for SnS_2/CdS heterostructures.

consumed by reacting with the sacrificial agent in the valence band of SnS_2, which helps inhibit the photocorrosion phenomenon of CdS. Therefore, the charge transfer mechanism of the S-scheme heterostructure endowed the SnS_2/CdS with a higher reducing capacity for the photocatalytic hydrogen evolution.

To deeply analyse the transfer direction of electrons in the SnS_2/CdS heterostructures, the work function (Φ_{DFT}), density state of density (DOS), hydrogen adsorption free energy (ΔG_{H^*}) and differential charge density of CdS, SnS_2, SnS_2/CdS heterostructures were calculated by density functional theory (DFT) (Fig. 9). The work function of the CdS (002), SnS_2 (100), and SnS_2/CdS models (Fig. S12†) was calculated by the first-principles simulation using the equation $\Phi_{DFT} = E_{vac} - E_F$.[58] According to the crystal models, the work functions of CdS (002), SnS_2 (100), and the SnS_2/CdS interface were calculated to be 5.791, 6.683, and 6.249 eV, respectively. This is consistent with the distribution of the conduction and valence band potentials of CdS and SnS_2 measured by experiments, which once again proved that SnS_2/CdS heterostructures conform to the S-scheme electron transfer mechanism. From the DOS calculation results of SnS_2/CdS heterostructures, it can be seen that the density of states near the Fermi level is mainly composed of the Cd element in CdS. Meanwhile, CdS is more involved in the photocatalytic hydrogen evolution reaction, and the S element in CdS is the main catalytically active site.[59,60] On comparing the PDOS of the SnS_2/CdS heterostructures and pure CdS, the density of states below the Fermi level (valence band) of the S element of CdS in the SnS_2/CdS heterostructures was significantly higher than that of the S element in pure CdS, indicating that CdS gained electrons from SnS_2. Similarly, compared with the density of Sn states in SnS_2 of SnS_2/CdS heterostructures and pure SnS_2, the density of Sn states above the Fermi level (conduction band) of Sn elements in SnS_2 of the SnS_2/CdS heterostructures is lower than that of Sn elements in pure SnS_2, which proves that the empty orbital composition of SnS_2 increases and electrons are transferred outward to CdS. Based on the above results, the electrons in the SnS_2/CdS heterostructures are transferred from the conduction band of SnS_2 to the valence band of CdS under the action of the built-in electric field. To evaluate the activity of photocatalysts, the hydrogen adsorption free energy (ΔG_{H^*}) as an important index was calculated.[61] The closer the ΔG_{H^*} value is to zero, the easier for H* to be adsorbed on the surface of the catalyst, which is beneficial for H_2 evolution. The ΔG_{H^*} value of the SnS_2/CdS heterostructures is closer to zero as compared with those of pure CdS and SnS_2, suggesting that constructing 2D–2D strongly coupled heterostructures is a feasible method for improving the hydrogen evolution performance of photocatalysts. In addition, according to the charge density difference diagram (Fig. 9h and S13†) and charge density diagram (Fig. S14†) of CdS (002), SnS_2 (100), and SnS_2/CdS heterostructures,[62] the S element in CdS at the interface of SnS_2/CdS gain the most electrons, which further indicates that the S site in CdS is the main active site of the hydrogen evolution reaction.

4. Conclusions

In summary, strongly coupled 2D–2D SnS_2/CdS S-scheme heterostructures were constructed by a hydrothermal method. The SnS_2 NSs were uniformly inserted into the lacunas of CdS NSs to form tight face-to-face contact. Benefiting from the abundant active sites and high-efficiency charge separation, the obtained SnS_2/CdS S-scheme heterostructures exhibited excellent photocatalytic performance and remarkable stability. Moreover, the large contact area and strongly coupled interplay elevated the charge kinetics. With lactic acid as the sacrificial agent, the highest hydrogen evolution rate of SnS_2/CdS heterostructures was 5.18 mmol g^{-1} h^{-1}, and the corresponding AQE was 59.3% at 420 nm. When the sacrificial agent was changed from lactic acid to methanol, a hydrogen production rate of 3.27 mmol g^{-1} h^{-1} was obtained, and the methanol was oxidized to CH_3OCH_2OH. Combining the detailed analyses of XPS valences and optical band gaps, the carrier transfer mechanism of the S-scheme heterostructure is well explained. This work offers an effective strategy for constructing strongly coupled 2D–2D S-scheme heterostructures to accelerate charge transfer for solar-driven reactions.

Conflicts of interest

There are no conflicts to declare.

Acknowledgements

We thank the financial support from the National Natural Science Foundation of China (No. 21871065 and 22071038), Heilongjiang Touyan Team (HITTY-20190033), and Interdisciplinary Research Foundation of HIT (IR2021205).

Notes and references

1 S. Wang, Y. Wang, S. L. Zhang, S. Q. Zang and X. W. Lou, Supporting Ultrathin $ZnIn_2S_4$ Nanosheets on Co/N-Doped Graphitic Carbon Nanocages for Efficient Photocatalytic H_2 Generation, *Adv. Mater.*, 2019, **31**, 1903404.
2 C. Liu, P. Wu, J. Wu, J. Hou, H. Bai and Z. Liu, Effective protect of oxygen vacancies in carbon layer coated black TiO_{2-x}/CNNS hetero-junction photocatalyst, *Chem. Eng. J.*, 2019, **359**, 58–68.
3 H. Wang, L. Zhang, Z. Chen, J. Hu, S. Li, Z. Wang, J. Liu and X. Wang, Semiconductor heterojunction photocatalysts: design, construction, and photocatalytic performances, *Chem. Soc. Rev.*, 2014, **43**, 5234–5244.
4 T. Hisatomi and K. Domen, Reaction systems for solar hydrogen production via water splitting with particulate semiconductor photocatalysts, *Nat. Catal.*, 2019, **2**, 387–399.
5 W. Wang, X. Zhao, Y. Cao, Z. Yan, R. Zhu, Y. Tao, X. Chen, D. Zhang, G. Li and D. Phillips, Copper phosphide-enhanced lower charge trapping occurrence in graphitic-C_3N_4 for efficient noble-metal-free photocatalytic H_2 evolution, *ACS Appl. Mater. Interfaces*, 2019, **11**, 16527–16537.

6 J. Chen, X. J. Wu, L. Yin, B. Li, X. Hong, Z. Fan, B. Chen, C. Xue and H. Zhang, One-pot synthesis of CdS nanocrystals hybridized with single-layer transition-metal dichalcogenide nanosheets for efficient photocatalytic hydrogen evolution, *Angew. Chem., Int. Ed.*, 2015, **127**, 1226–1230.

7 Y. Hu, X. Hao, Z. Cui, J. Zhou, S. Chu, Y. Wang and Z. Zou, Enhanced photocarrier separation in conjugated polymer engineered CdS for direct Z-scheme photocatalytic hydrogen evolution, *Appl. Catal., B*, 2020, **260**, 118131.

8 J. Y. Li, Y. H. Li, F. Zhang, Z. R. Tang and Y. Xu, Visible-light-driven integrated organic synthesis and hydrogen evolution over 1D/2D CdS-$Ti_3C_2T_x$ MXene composites, *Appl. Catal., B*, 2020, **269**, 118783.

9 M. Xiong, J. Yan, B. Chai, G. Fan and G. Song, Liquid exfoliating CdS and MoS_2 to construct 2D/2D MoS_2/CdS heterojunctions with significantly boosted photocatalytic H_2 evolution activity, *J. Mater. Sci. Technol.*, 2020, **56**, 179–188.

10 B. Sun, P. Qiu, Z. Liang, Y. Xue, X. Zhang, L. Yang, H. Cui and J. Tian, The fabrication of 1D/2D CdS nanorod@Ti_3C_2 MXene composites for good photocatalytic activity of hydrogen generation and ammonia synthesis, *Chem. Eng. J.*, 2021, **406**, 127177.

11 Y. Lu, Y. Li, Y. Wang and J. Zhang, Two-photon induced NIR active core-shell structured WO_3/CdS for enhanced solar light photocatalytic performance, *Appl. Catal., B*, 2020, **272**, 118979.

12 P. Devaraji, R. Gao, L. Xiong, X. Jia, L. Huang, W. Chen, S. Liu and L. Mao, Usage of natural leaf as a bio-template to inorganic leaf: Leaf structure black TiO_2/CdS heterostructure for efficient photocatalytic hydrogen evolution, *Int. J. Hydrogen Energy*, 2021, **46**, 14369–14383.

13 Y. Chen, J. F. Li, P. Y. Liao, Y. S. Zeng, Z. Wang and Z. Q. Liu, Cascaded electron transition in $CuWO_4$/CdS/CDs heterostructure accelerating charge separation towards enhanced photocatalytic activity, *Chin. Chem. Lett.*, 2020, **31**, 1516–1519.

14 H. Yu, F. Chen, F. Chen and X. Wang, In situ self-transformation synthesis of g-C_3N_4-modified CdS heterostructure with enhanced photocatalytic activity, *Appl. Surf. Sci.*, 2015, **358**, 385–392.

15 L. Zou, H. Wang and X. Wang, High efficient photodegradation and photocatalytic hydrogen production of CdS/$BiVO_4$ heterostructure through Z-scheme process, *ACS Sustainable Chem. Eng.*, 2017, **5**, 303–309.

16 Y. P. Xie, Y. Yang, G. Wang and G. Liu, Oxygen vacancies promoted interfacial charge carrier transfer of CdS/ZnO heterostructure for photocatalytic hydrogen generation, *J. Colloid Interface Sci.*, 2017, **503**, 198–204.

17 L. Li, C. Guo, J. Ning, Y. Zhong, D. Chen and Y. Hu, Oxygen-vacancy-assisted construction of FeOOH/CdS heterostructure as an efficient bifunctional photocatalyst for CO_2 conversion and water oxidation, *Appl. Catal., B*, 2021, **293**, 120203.

18 G. Wang, L. Gong, Z. Li, B. Wang, W. Zhang, B. Yuan, T. Zhou, X. Long and A. Kuang, A two-dimensional CdO/CdS heterostructure used for visible light photocatalysis, *Phys. Chem. Chem. Phys.*, 2020, **22**, 9587–9592.

19 X. Li, C. Garlisi, Q. Guan, S. Anwer, K. Al-Ali, G. Palmisano and L. Zheng, A review of material aspects in developing direct Z-scheme photocatalysts, *Mater. Today*, 2021, **47**, 75–107.

20 M. Liu, L. Z. Qiao, B. B. Dong, S. Guo, S. Yao, C. Li, Z. M. Zhang and T. B. Lu, Photocatalytic coproduction of H_2 and industrial chemical over MOF-derived direct Z-scheme heterostructure, *Appl. Catal., B*, 2020, **273**, 119066.

21 Z. Zhang, J. Huang, M. Zhang, Q. Yuan and B. Dong, Ultrathin hexagonal SnS_2 nanosheets coupled with g-C_3N_4 nanosheets as 2D/2D heterojunction photocatalysts toward high photocatalytic activity, *Appl. Catal., B*, 2015, **163**, 298–305.

22 Y. J. Yuan, Z. Shen, S. Wu, Y. Su, L. pei, Z. Ji, M. Ding, W. Bai, Y. Chen, Z. Yu and Z. Zou, Liquid exfoliation of g-C_3N_4 nanosheets to construct 2D-2D MoS_2/g-C_3N_4 photocatalyst for enhanced photocatalytic H_2 activity, *Appl. Catal., B*, 2019, **246**, 120–128.

23 Z. Zhang, J. Huang, M. Zhang, Q. Yuan and B. Dong, Ultrathin hexagonal SnS_2 nanosheets coupled with g-C_3N_4 nanosheets as 2D/2D heterojunction photocatalysts toward high photocatalytic activity, *Appl. Catal., B*, 2015, **163**, 298–305.

24 J. Yu, C. Y. Xu, F. X. Ma, S. P. Hu, Y. W. Zhang and L. Zhen, Monodisperse SnS_2 nanosheets for high-performance photocatalytic hydrogen generation, *ACS Appl. Mater. Interfaces*, 2014, **6**, 22370–22377.

25 T. Qiang, L. Chen, Y. Xia and X. Qin, Dual modified MoS_2/SnS_2 photocatalyst with Z-scheme heterojunction and vacancies defects to achieve a superior performance in Cr (VI) reduction and dyes degradation, *J. Cleaner Prod.*, 2021, **291**, 125213.

26 H. She, H. Zhou, L. Li, Z. Zhao, M. Jiang, J. Huang, L. Wang and Q. Wang, Construction of a Two-Dimensional Composite Derived from TiO_2 and SnS_2 for Enhanced Photocatalytic Reduction of CO_2 into CH_4, *ACS Sustainable Chem. Eng.*, 2019, **7**, 650–659.

27 C. Liu, Z. Dong, C. Yu, J. Gong, Y. Wang, Z. Zhang and Y. Liu, Study on photocatalytic performance of hexagonal SnS_2/g-C_3N_4 nanosheets and its application to reduce U (VI) in sunlight, *Appl. Surf. Sci.*, 2021, **537**, 147754.

28 Y. Li, B. Yu, Z. Hu and H. Wang, Construction of direct Z-scheme SnS_2@$ZnIn_2S_4$@kaolinite heterostructure photocatalyst for efficient photocatalytic degradation of tetracycline hydrochloride, *Chem. Eng. J.*, 2022, **429**, 132105.

29 L. Zhang, C. G. Niu, X. J. Wen, H. Guo, X. F. Zhao, C. Liang and G. M. Zeng, Enhanced photocatalytic activity of CdS/SnS_2 nanocomposite with highly-efficient charge transfer and visible light utilization for selective reduction of 4-nitroaniline, *J. Colloid Interface Sci.*, 2018, **532**, 557–570.

30 L. Long, G. Lv, Q. Han, X. Wu, Y. Qian, D. Wang, Y. Zhou and Z. Zou, Achieving Direct Z-Scheme Charge Transfer through Constructing 2D/2D α-Fe_2O_3/CdS Heterostructure for Efficient Photocatalytic CO_2 Conversion, *J. Phys. Chem. C*, 2021, **125**, 23142–23152.

31 J. Chu, X. Han, Z. Yu, Y. Du, B. Song and P. Xu, Highly efficient visible-light-driven photocatalytic hydrogen production on $CdS/Cu_7S_4/g\text{-}C_3N_4$ ternary heterostructures, *ACS Appl. Mater. Interfaces*, 2018, **10**, 20404–20411.

32 B. Sun, J. Bu, X. Chen, D. Fan, S. Li, Z. Li, W. Zhou and Y. Du, In-situ interstitial zinc doping-mediated efficient charge separation for $ZnIn_2S_4$ nanosheets visible-light photocatalysts towards optimized overall water splitting, *Chem. Eng. J.*, 2022, 135074.

33 Y. Liu, Y. Zhou, X. Zhou, X. Jin, B. Li, J. Liu and G. Chen, Cu doped SnS_2 nanostructure induced sulfur vacancy towards boosted photocatalytic hydrogen evolution, *Chem. Eng. J.*, 2021, **407**, 127180.

34 Z. Ai, G. Zhao, Y. Zhong, Y. Shao, B. Huang, Y. Wu and X. Hao, Phase junction CdS: high efficient and stable photocatalyst for hydrogen generation, *Appl. Catal., B*, 2018, **221**, 179–186.

35 J. Zhang, L. Zhang, Y. Shi, G. Xu, E. Zhang, H. Wang, Z. Kong, J. Xi and Z. Ji, Anatase TiO_2 nanosheets with coexposed {101} and {001} facets coupled with ultrathin SnS_2 nanosheets as a face-to-face npn dual heterojunction photocatalyst for enhancing photocatalytic activity, *Appl. Surf. Sci.*, 2017, **420**, 839–848.

36 T. Sriv, K. Kim and H. Cheong, Low-frequency Raman spectroscopy of few-layer 2H-SnS_2, *Sci. Rep.*, 2018, **8**, 1–7.

37 L. Dashairya, M. Sharma, S. Basu and P. Saha, SnS_2/RGO based nanocomposite for efficient photocatalytic degradation of toxic industrial dyes under visible-light irradiation, *J. Alloys Compd.*, 2019, **774**, 625–636.

38 D. Shang, D. Li, B. Chen, B. Luo, Y. Huang and W. Shi, 2D–2D SnS_2/Covalent Organic Framework Heterojunction Photocatalysts for Highly Enhanced Solar-Driven Hydrogen Evolution without Cocatalysts, *ACS Sustainable Chem. Eng.*, 2021, **9**, 14238–14248.

39 S. Wang, X. Zhao, H. M. A. Sharif, Z. Chen, Y. Chen, B. Zhou, K. Xiao, B. Yang and Q. Duan, Amine-CdS for exfoliating and distributing bulk MoO_3 for photocatalytic hydrogen evolution and Cr (VI) reduction, *Chem. Eng. J.*, 2021, **406**, 126849.

40 P. Li, W. Fu, P. Zhuang, Y. Cao, C. Tang, A. B. Watson, P. Dong, J. Shen and M. Ye, Amorphous Sn/crystalline SnS_2 nanosheets via in situ electrochemical reduction methodology for highly efficient ambient N2 fixation, *Small*, 2019, **15**, 1902535.

41 F. Guo, H. Sun, Y. Shi, F. Zhou and W. Shi, CdS nanoparticles decorated hexagonal Fe_2O_3 nanosheets with a Z-scheme photogenerated electron transfer path for improved visible-light photocatalytic hydrogen production, *Chin. J. Chem. Eng.*, 2022, **43**, 266–274.

42 I. Shown, S. Samireddi, Y. Chang, R. Putikam, P. Chang, A. Sabbah, F. Fu, W. Chen, C. Wu, T. Yu, P. Chung, M. Lin, L. Chen and K. Chen, Carbon-doped SnS_2 nanostructure as a high-efficiency solar fuel catalyst under visible light, *Nat. Commun.*, 2018, **9**, 1–10.

43 M. Cruz, J. Morales, J. P. Espinos and J. Sanz, XRD, XPS and ^{119}Sn NMR study of tin sulfides obtained by using chemical vapor transport methods, *J. Solid State Chem.*, 2003, **175**, 359–365.

44 T. Jiang and G. A. Ozin, Tin (IV) sulfide-alkylamine composite mesophase: a new class of thermotropic liquid crystals, *J. Mater. Chem.*, 1997, **7**, 2213–2222.

45 D. J. Kubicki, D. Prochowicz, E. Salager, A. Rakhmatullin, C. Grey, L. Emsley and S. D. Stranks, Local structure and dynamics in methylammonium, formamidinium, and cesium Tin (II) mixed-halide perovskites from ^{119}Sn Solid-state NMR, *J. Am. Chem. Soc.*, 2020, **142**, 7813–7826.

46 L. Choubrac, M. Paris, A. Lafond, C. G. Deudon, X. Rocquefelte and S. Jobic, Multinuclear (^{67}Zn, ^{119}Sn and ^{65}Cu) NMR spectroscopy-an ideal technique to probe the cationic ordering in Cu_2ZnSnS_4 photovoltaic materials, *Phys. Chem. Chem. Phys.*, 2013, **15**, 10722–10725.

47 B. Zheng, X. Liu, J. Zhu, Z. Jun, G. Zhong, Y. Xiang, H. Wang, W. Zhao, E. Umeshbabu, Q. Wu, J. Huang and Y. Yang, Unraveling (electro)-chemical stability and interfacial reactions of $Li_{10}SnP_2S_{12}$ in all-solid-state Li batteries, *Nano Energy*, 2020, **67**, 104252.

48 X. Zhang, T. Liu, F. Zhao, N. Zhang and Y. Wang, In-situ-formed Cd and Ag_2S decorated CdS photocatalyst with boosted charge carrier spatial separation for enhancing UV-vis-NIR photocatalytic hydrogen evolution, *Appl. Catal., B*, 2021, **298**, 120620.

49 Y. Huo, Y. Yang, K. Dai and J. Zhang, Construction of 2D/2D porous graphitic C_3N_4/SnS_2 composite as a direct Z-scheme system for efficient visible photocatalytic activity, *Appl. Surf. Sci.*, 2019, **481**, 1260–1269.

50 G. Liu, H. Zhao, F. Diao, Z. Ling and Y. Wang, Stable tandem luminescent solar concentrators based on CdSe/CdS quantum dots and carbon dots, *J. Mater. Chem. C*, 2018, **6**, 10059–10066.

51 K. E. Hughes, K. H. Hartstein and D. R. Gamelin, Photodoping and transient spectroscopies of copper-doped CdSe/CdS nanocrystals, *ACS Nano*, 2018, **12**, 718–728.

52 Y. Fan, W. Zhou, X. Qiu, H. Li, Y. Jiang, Z. Sun, D. Han, L. Niu and Z. Tang, Selective photocatalytic oxidation of methane by quantum-sized bismuth vanadate, *Nat. Sustain.*, 2021, **4**, 509–515.

53 Y. Xu, Y. Zhou, J. Guo, S. Zhang and Y. Lu, Preparation of $SnS_2/g\text{-}C_3N_4$ composite as the electrode material for Supercapacitor, *J. Alloys Compd.*, 2019, **806**, 343–349.

54 L. Meng, X. Zhou, S. Wang, Y. Zhou, W. Tian, P. Kidkhunthod, S. Tunmee, Y. Tang, R. Long and Y. Xin, A Plasma-Triggered O-S Bond and P-N Junction Near the Surface of a SnS_2 Nanosheet Array to Enable Efficient Solar Water Oxidation, *Angew. Chem., Int. Ed.*, 2019, **58**, 16668–16675.

55 Y. Zuo, Y. Liu, J. Li, R. Du, X. Yu, C. Xing, T. Zhang, L. Yao, J. Arbiol, J. Llorca, K. Sivula, N. Guijarro and A. Cabot, Solution-processed ultrathin SnS_2-Pt nanoplates for photoelectrochemical water oxidation, *ACS Appl. Mater. Interfaces*, 2019, **11**, 6918–6926.

56 J. Xu, S. Lai, M. Hu, S. Ge, R. Xie, F. Li, D. Hua, H. Xu, H. Zhou, R. Wu, J. Fu, Y. Qiu, H. Jia, C. Li, H. Liu, Y. Liu, J. Sun, X. Liu and J. Luo, Semimetal 1H-SnS_2 Enables

High-Efficiency Electroreduction of CO_2 to CO, *Small Methods*, 2020, **4**, 2000567.

57 Q. Zhou, L. Zhang, L. Zhang, B. Jiang and Y. Sun, In-situ constructed 2D/2D $ZnIn_2S_4/Bi_4Ti_3O_{12}$ S-scheme heterojunction for degradation of tetracycline: Performance and mechanism insights, *J. Hazard. Mater.*, 2022, **438**, 129438.

58 R. Jacobs, J. Booske and D. Morgan, Understanding and controlling the work function of perovskite oxides using density functional theory, *Adv. Funct. Mater.*, 2016, **26**, 5471–5482.

59 M. Guo, M. Ji and W. Cui, Theoretical investigation of HER/OER/ORR catalytic activity of single atom-decorated graphyne by DFT and comparative DOS analyses, *Appl. Surf. Sci.*, 2022, **592**, 153237.

60 S. Silver, J. Yin, H. Li, J. Brédas and A. Kahn, Characterization of the valence and conduction band levels of n= 1 2D perovskites: a combined experimental and theoretical investigation, *Adv. Energy Mater.*, 2018, **8**, 1703468.

61 Y. Cheng, X. Fan, F. Liao, S. Lu, Y. Lu, L. B. Li, Y. Q. Liu, H. P. Li, M. W. Lin and S. T. Lee, Os/Si nanocomposites as excellent hydrogen evolution electrocatalysts with thermodynamically more favorable hydrogen adsorption free energy than platinum, *Nano Energy*, 2017, **39**, 284–290.

62 U. Das, G. Zhang, B. Hu, A. S. Hock, P. C. Redfern, J. T. Miller and L. A. Curtiss, Effect of siloxane ring strain and cation charge density on the formation of coordinately unsaturated metal sites on silica: insights from density functional theory (DFT) studies, *ACS Catal.*, 2015, **5**, 7177–7185.